doi:10.3723/QGFH2448

Seismic soil-monopile-structure interaction for offshore wind turbines: from 3D to 1D modelling

D. Delavinia
GR8 GEO, Athens, Greece (formerly Delft University of Technology, Delft, the Netherlands)

E. Kementzetzidis
Delft University of Technology, Delft, the Netherlands

S. Panagoulias
Delft University of Technology, Delft, the Netherlands
Siemens Gamesa Renewable Energy, The Hague, the Netherlands

A. Tsouvalas & F. Pisanò
Delft University of Technology, Delft, the Netherlands

ABSTRACT: To accommodate the foreseen expansion of the offshore wind sector, monopile-supported Offshore Wind Turbines (OWTs) are currently being designed for harvesting offshore wind energy in seismically active regions. Three-dimensional (3D) Finite Element (FE) analyses have proven a reliable, though computationally expensive, tool for modelling laterally loaded monopiles. A more efficient modelling approach is the one-dimensional (1D) Beam-on-Winkler-Foundation (BWF) method, where the monopile is modelled via a series of beam elements, laterally supported by uncoupled, lateral soil springs. Under the simplifying assumption of linear elastic soil behaviour, this study explores the suitability of the BWF method for the simulation of the seismic soil-structure interaction by comparing the response obtained through 1D modelling to the outcome of 3D FE calculations. To this end, different monopile geometries are examined, for which the contributions of multiple soil resisting mechanisms (determined by normal and tangential stresses along the pile shaft and base) to the global monopile response are also assessed.

1 Introduction

Monopiles for Offshore Wind Turbines (OWTs) are tubular steel piles with large diameters (D), typically higher than 5m, relatively short embedded lengths (L) (Kaynia, 2020) and L/D ratios usually ranging between 3 and 8. They are the most common foundation option (Wind Europe, 2020) owing to their simple and cost-effective design, together with the vast knowledge accumulated and still expanding with regard to their installation and related installation effects (Kementzetzidis, 2023; Tsetas et al., 2023).

Currently, the offshore wind market is expanding to the seismically active areas of the Asia-Pacific region and the North America (Bhattacharya et al., 2021; GWEC, 2022). Such an expansion would require from offshore engineers to design monopiles as support structures of OWTs for a new set of loading conditions. Furthermore, recent research findings (Medina et al., 2021) support that seismic loading conditions are expected to define the foundation design, only adding to the relevance of studies concerning seismic soil-monopile interactions.

Seismic analyses can accurately be performed via three-dimensional (3D) Finite Element (FE) models, which are however relatively complex and computationally expensive. On the other hand, one-dimensional (1D) FE modelling of seismic soil-structure interaction is simpler and faster; therefore, it potentially provides a valuable, user-friendly option for the seismic design of monopile-supported OWTs.

A common approach to the 1D modelling of soil-structure interaction is based on the Beam-on-Winkler-Foundation (BWF) assumption, where the monopile is modelled with 1D beam elements connected to the soil through lateral load-displacement (p-y) springs; each spring describes the variation of the lateral soil reaction per unit pile length with the local (pile) lateral deflection. This approach has proven suitable in case of flexible piles, with international codes of practice providing recommendations for p-y reaction curves based on soil properties (API, 2011; DNVGL, 2016).

Monopiles of low L/D, that are currently used in the offshore wind industry, have been designed to rotate as (relatively) rigid bodies under the action of lateral loads. As a result, meaningful vertical shear stresses from the surrounding soil develop at the pile periphery which induce distributed moments down the embedded depth (Byrne et al., 2015). To capture this effect, enforcing the reaction profile with distributed moment-rotation (m-θ) springs has been suggested (Byrne et al., 2015; Wan et al., 2021). In addition, two other resistant mechanisms will become important as the L/D ratio decreases, namely the base shear and moment (He et al., 2021), which can still be modelled via lumped base reactions (Byrne et al., 2015, Wan et al., 2021).

In this study, the contribution of each of the aforementioned resisting mechanisms in the prediction of the 3D seismic soil-structure interaction is examined by comparing the results of 3D and 1D FE calculations. The elastodynamic system response is examined by assigning linear elastic properties to all system components. Future steps could investigate the impact of employing soil nonlinearity for the 3D soil continuum (Vacareanu et al., 2019) and the local soil reactions using available nonlinear cyclic models (Dafalias & Manzari, 2004; Kementzetzidis et al., 2022).

The system properties and the numerical methodology both for 3D and 1D analyses are described in Section 2. In Section 3, the calibration procedure for the individual spring stiffnesses is presented along with the ensuing analysis results. Section 4 discusses the contribution of the additional soil reaction components to the prediction of the 3D dynamic interaction as a function of the loading frequency (i.e., under monoharmonic excitation and in steady-state conditions) and concludes on the effectiveness of the hereby calibrated p-y and m-θ springs. In Section 5, the suitability of the 1D model to simulate realistic (i.e., transient) earthquake loading is examined. Lastly, in Section 6, conclusions are drawn regarding the applicability of 1D FE modelling for representing the fully 3D response of the system at hand.

2 Methodology

This study investigates the seismic behaviour of monopiles under the assumption of linear elasticity for all the system components (i.e., structure and soil). A uniform, 50m-thick soil layer was considered, overlaying a rigid bedrock. The shear modulus (G_{soil}) and bulk density (ρ_{soil}) were taken equal to 106MPa and 1.84Mg/m^3, respectively, yielding a shear wave velocity (V_{soil}) of 240m/s. A Poisson's ratio (ν) of 0.30 was assumed.

To examine the relative contribution of the four reaction components (Section 1), three monopiles with different geometries were simulated, as shown in Table 1. Above mudline, a steel structure was modelled (E_{steel}=210GPa and mass per length=0.37Mg/m), with a 50Mg nodal mass at the top, 8m length, 0.67m diameter and 19mm wall thickness, which, given the low mass per length and high nodal mass on top, behaves similarly to a Single Degree of Freedom (SDOF) system.

Table 1: Monopile properties

Length (L, m)	Diameter (D, m)	L/D (-)	Wall thickness (mm)
17.5	0.67	26	19
17.5	2.0	9	20
36.0	7.5	5	75

2.1 *3D FE modelling*

The 3D FE analyses were performed using the FE software OpenSees (McKenna et al., 2010), and the graphical user interface OpenSeesPL (Lu et al., 2011) where half the real problem is simulated to decrease the duration of the analyses. The soil continuum was modelled using single-phase 8-node standard brick ('8-node std-Brick') elements, while the structure was simulated using 1D linear Timoshenko beam elements. Monopile and soil were considered fully bonded (He et al., 2021; Wan et al., 2021). Below the soil surface, the pile-soil compatibility was enforced via multiple horizontal rigid links that connect the beam nodes to the surrounding soil nodes, simulating the area occupied by the monopile.

The shear beam boundary condition was applied at the lateral boundaries of the model (i.e., nodes of the same depth have the same lateral and vertical displacements, known as 'tied-node' boundary condition), while the vertical displacements at the bottom of the layer were fixed to simulate the underlying rigid rock. The domain size was determined based on the results of specific sensitivity analyses. The lateral boundaries were placed at a 25D-distance from the pile centerline, which has proven sufficient to minimize any boundary effects.

The maximum vertical element size (dz_{max}) was defined as the minimum shear wavelength (of interest) to be transmitted into the soil layer divided by ten (Watanabe et al., 2017). The maximum time-step size was then calculated as dz_{max} / V_{soil} to guarantee the accuracy of the solution (stability was ensured via the employment of the unconditionally stable scheme), ensuring that waves may not artificially reach two nodes at the same time (Watanabe et al., 2017). In the horizontal direction, the mesh discretization was set to be finer close to the pile, and gradually coarser towards the lateral boundaries. The FE mesh in case of L/D=9 is shown in Figure 1.

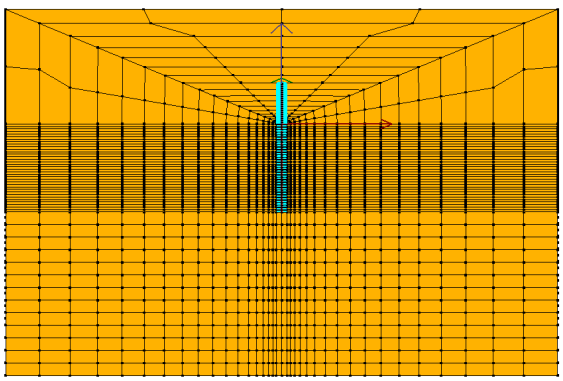

Figure 1: FE mesh in OpenSeesPL for L/D=9

The model was excited at the rigid bottom and the analyses were performed in the time domain. Rayleigh damping was considered to simulate a practically constant 5% material (viscous) damping

ratio throughout the frequency range of interest, with f_1 and f_2 being equal to 1 and 10Hz, respectively.

2.2 *Engineering modelling*

For the 1D modelling of dynamic soil-structure interaction, shear wave propagation in the free-field must be first considered. In OpenSees, 1D site response analyses were first performed (assuming vertically propagating shear waves) and secondly, the seismic soil-structure interaction analyses were conducted.

As far as the distributed translational (*p-y*) springs are concerned, the calculated total lateral displacements over depth were applied to the supports (i.e., free field end) of the springs (Boulanger et al., 1999; Rahmani et al., 2018). In addition, when considering *m-θ* springs, the rotations resulting from the shear deformation of the soil column -under the vertical propagation of shear waves- were applied at the supports of these springs, similarly to the procedure followed in case of caisson foundations (Gerolymos & Gazetas, 2006).

Regarding the space discretization of the 1D models, the maximum vertical element size was calculated as the minimum between: (a) the size based on the already presented 'rules of thumb' (Section 2.1) and (b) the beam element size for which convergence of the pile head (i.e., at mudline) deflection was reached under monotonic pile head loading (Section 3). The maximum timestep was calculated similarly to 3D (Section 2.1).

Material (viscous) damping was accounted for by considering a Rayleigh damping with 5% damping ratio defined at the same frequencies f_1 and f_2 as in 3D (Section 2.1).

2.2.1 *1D site response analysis*

The 1D soil column was modelled via a series of plane strain quadrilateral elements and the 'tied-node' boundary condition was employed, as in 3D (Section 2.1). Seismic shaking was introduced by imposing selected acceleration signals at the base of the column, which was fixed in the vertical direction.

2.2.2 *1D seismic soil-structure interaction*

Both monopile and structure were modelled via 1D linear Timoshenko beam elements, as in 3D. Radiation damping was ignored (i.e., no dashpots were considered), in line with the work of Anoyatis et al. (2013), who examined the kinematic interaction of piles and concluded that the approximate representation of the radiation damping based on planar wave-propagation analysis (Gazetas & Dobry, 1984) results in a mismatch between the 3D and 1D calculations for frequencies higher than the cut-off frequency (i.e., first natural frequency) of the soil layer. Conversely, the same study indicated that solely considering the static spring stiffness coefficient resulted in a good match between the 3D and 1D prediction of the soil-monopile kinematic interaction no matter the excitation frequency.

3 **From 3D-to-1D: spring stiffness calibration**

The distributed lateral (*p-y*) and rotational (*m-θ*) linear elastic springs were calibrated based on monotonic loading, applying a lateral force and moment at the pile head, respectively. Note that $p/y = k_y$ and $m/\theta = k_\theta$, *where* k_y (with units of stress) is the *p-y* elastic spring stiffness, and k_θ (with units of force) the *m-θ* elastic rotational stiffness.

The lateral (k_y) and rotational (k_θ) spring stiffnesses were considered uniformly distributed along the pile length, except for the springs both at the pile head and tip, where half the spring stiffness was assigned (Griffiths, 1989). Following numerical convergence studies, both for the distributed translational and rotational springs, the vertical spacing was defined equal to 0.25m.

This section provides different calibration procedures of k_y and k_θ. Their effectiveness in capturing the 3D response of the system is examined in Sections 4 and 5. With respect to the base shear and moment, a base lateral and rotational spring were examined, respectively, by applying already existing formulations (Section 4.3).

3.1 *Distributed lateral p-y springs*

Two different k_y values were defined so that agreement between 3D and 1D optimized in terms of either the monotonic pile head or average-over-depth pile deflection. These stiffnesses are denoted by $k_{y,h}$ and $k_{y,a}$, respectively.

Figure 2 illustrates the variation of the dimensionless ratios $k_{y,a} / G_{soil}$ and $k_{y,h} / G_{soil}$ versus the *L/D* aspect ratio. Expressing the lateral spring stiffness k_y as proportional to G_{soil} is a common approach in the literature (Randolph & Gourvenec, 2011; Wan et al., 2021). It is observed that for both calibration methods, a negative correlation with *L/D* exists, with the *p-y* spring stiffness increasing as the *L/D* decreases, in agreement with the observations of Wan et al. (2021).

In particular, $k_{y,a} / G_{soil}$ equals 2.8 for the most slender pile examined herein (i.e., *L/D*=26) and 3.8 for the most rigid (i.e., *L/D*=5). In the case of the lateral spring stiffness which matches the pile head deflection between 3D and 1D (i.e., $k_{y,h} / G_{soil}$), the corresponding values are 6.5 and 7.5, respectively. The examples considered here suggest that for the same *L/D* value, $k_{y,h}$ is always larger than $k_{y,a}$. Regarding the monopile with *L/D*=5, $k_{y,h} / G_{soil}$ is practically identical to Wan et al. (2021).

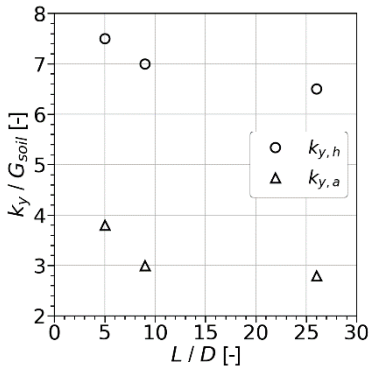

Figure 2: Variation of k_y / G_{soil} with L/D for different calibration procedures

3.2 *Distributed rotational m-θ springs*

To calibrate the *m-θ* spring stiffness, the previously calibrated *p-y* springs (Section 3.1) were accounted for. For each monopile, three different k_θ values were defined depending on the k_y spring stiffness that was considered (i.e., $k_{y,h}$ or $k_{y,a}$) and the target 3D rotation (i.e., pile head rotation or average-over-depth pile rotation).

The first rotational stiffness to be defined, denoted by $k_{\theta,h\text{-}h}$, optimized the agreement between 3D and 1D in case of the pile head rotation under monotonic pile head moment loading, while accounting for the distributed lateral stiffness $k_{y,h}$ (Section 3.1). The second rotational stiffness, denoted by $k_{\theta,a\text{-}a}$, aimed at minimizing the discrepancy between 3D and 1D in terms of the average-over-depth rotation, while considering the lateral stiffness $k_{y,a}$ (Section 3.1). Lastly, the third rotational stiffness, denoted as $k_{\theta,h\text{-}a}$, targeted the 3D and 1D match of the average-over-depth pile rotation when *p-y* springs with $k_{y,h}$ were considered.

The distributed rotational stiffness was evaluated in terms of the dimensionless ratio k_θ / (G_{soil} D^2). Normalizing the rotational stiffness in this manner is a common procedure in case of caisson foundations (Gerolymos & Gazetas, 2006; Varun et al., 2009) and monopile foundations (Wan et al., 2021). No *m-θ* springs were calibrated in case of the slender monopile with L/D=26, as it will mainly bend laterally (with negligible rigid rotation) due to its large geometrical slenderness (Byrne et al., 2015). The identified values are presented in Table 2.

Table 2: Variation of k_θ / (G_{soil} D^2) with L/D for different calibration procedures

L/D	k_θ / G_{soil} D^2		
	$k_{\theta,h\text{-}h}$	$k_{\theta,a\text{-}a}$	$k_{\theta,h\text{-}a}$
9	2.3	2.5	1.3
5	2.3	2.5	1.3

According to Table 2, the dimensionless rotational coefficient k_θ / G_{soil} D^2 is independent of L/D. This is in contrast with the findings of Varun et al. (2009) and Wan et al. (2021) who made use of the four reaction components simultaneously. Further investigation for the L/D dependence of the k_θ / G_{soil} D^2 values is needed.

4 From 3D-to-1D: system dynamic response

The calculated spring stiffnesses (Section 3) were employed for the seismic simulation (i.e., base excitation) of soil-structure interaction effects at steady-state for different mono-harmonic bottom excitations. The 1D results were then compared to the 3D ones, in terms of the following dynamic interaction factors: (a) u_p / u_{ff}, where u_p is the steady-state pile deflection amplitude at mudline (i.e., pile head) and u_{ff} is the lateral displacement amplitude at the free-field, and (b) θ_p D / u_{ff}, where θ_p is the steady-state pile head rotation amplitude (i.e., at mudline), a common normalization scheme (Anoyatis et al., 2013; Fan & Gazetas, 1991). In addition, the moment and deflection distribution over depth for the 3D and 1D FE calculations were compared.

4.1 *1D modelling with lateral p-y springs only*

Figure 3 illustrates the dynamic pile head (i.e., at mudline) response in terms of u_p / u_{ff} for the monopiles with L/D equal to 26 and 5. The first natural frequency values, as calculated in 3D for the two systems (hereby denoted by $f_{0,SSI}$), are also noted with a grey dashed line. In the case of L/D=26, $f_{0,SSI}$ equals 0.93Hz, while for L/D=5, $f_{0,SSI}$ = 1.13Hz. According to this figure, a different excitation frequency results in a different dynamic response of the system (i.e., different u_p / u_{ff} values). Furthermore, different systems exhibit different dynamic responses for the same excitation frequency.

Local amplification and de-amplification of u_p relative to u_{ff} are observed around $f_{0,SSI}$ which are attributed to the structure on top of the monopile transitioning from an in-phase to an out-of-phase movement relative to the pile head (and free-field); hence the structure on top pushing the pile head forward or hindering its displacement, respectively. These effects are due to the inertial loading of the mass on top (Turner et al., 2017) and are more prominent for L/D=26 than for L/D=5, given the higher geometrical rigidity of the latter. They are referred to as 'inertial interaction' effects and affect the monopile response at shallow depths alone (Gazetas, 1984).

Regarding the 3D versus 1D comparison, in the case of L/D=26, the herewith employed *p-y* spring stiffnesses underpredict the first natural frequency of this system. In more detail, while $f_{0,SSI}$ equals 0.93Hz, the 1D FE models prediction is 0.87 and 0.83Hz in case of $k_{y,h}$ and $k_{y,a}$, respectively, resulting in errors equal to 6.5 and 11%. This can also be verified from Figure 3 where the local amplification/de-amplification area in 1D occurs earlier than in 3D.

However, it is observed that the *p-y* spring calibration selected to optimize the displacement at the pile head ($k_{y,h}$) predicts better u_p / u_{ff} values around the first natural frequency of the systems. Such a finding is unsurprising owing to the similarities between the inertial loading of the system on top of the monopile and the lateral loading at the pile head applied to calibrate $k_{y,h}$.

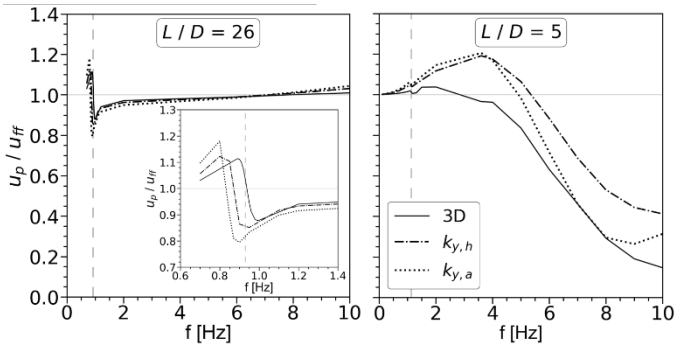

Figure 3: Comparison between the 3D and 1D FE modelling with *p-y* springs only of u_p / u_{ff} with frequency in case of bottom monoharmonic excitations, for monopiles with *L/D*=26 (right) and *L/D*=5 (left), including a zoom-in plot around $f_{0,SSI}$ for *L/D*=26

For the pile featuring *L/D*=5, the first natural frequency of the system is well-predicted by the 1D models. In particular, while $f_{0,SSI}$ equals 1.13Hz, the 1D models prediction is 1.12Hz, thus giving an error lower than 1%. Regarding the dynamic response with frequency, the following observations are made in comparison to the slender monopile with *L/D*=26: (a) the inertial interaction effects are lower (i.e., practically zero amplification/de-amplification), which is attributed to the stubbier monopile (*L/D*=5) being less affected by the inertial loading of the superstructure (same superstructure for all monopiles), and (b) the dynamic response is highly overestimated by the 1D models that make use of *p-y* springs only, given the monopile rotating as a relatively rigid body under lateral loading. Such a motion of the monopile enables the considerable contribution of additional reaction mechanisms; for instance, the distributed moment reaction (*m*) along the embedded monopile length.

Figure 4 illustrates the free-field and monopile deformation for $f_{0,SSI}$ (=1.13Hz) and higher excitation frequencies. It may be observed that, in the case of a 1.13Hz input, the monopile practically follows the soil layer deformation, while for a large frequency of 10Hz, the wavelength of the shear waves becomes shorter and the monopile geometrical rigidity hinders the monopile from following the deformation of the soil column. This seems to further complicate interaction effects in a manner that further highlights the importance of the *m-θ* soil reactions. These interaction effects between the soil layer and the monopile are termed 'kinematic interaction' effects (Turner et al., 2017) and influence the dynamics of the monopile all along its embedded length (Figure 4).

It should be noted that, for a particular soil layer, the frequency for which the kinematic interaction effects become important depends on the monopile geometrical rigidity. In addition, it should be acknowledged that although, in the case of relatively rigid monopiles, the kinematic interaction (i.e., deformation over depth) dictates the response for high excitation frequencies, the inertial interaction (i.e., deformation close to the surface) is still present resulting in an additional reduction of u_p / u_{ff} owing to the out-of-phase movement of the structure on top relative to the pile head and free-field.

At variance with the monopile with *L/D*=5, the monopile with *L/D*=26 follows the soil layer deformation throughout the frequency range, resulting in good predictions of the pile head dynamic response in the kinematic interaction area between the 3D and 1D FE models that make use of *p-y* springs only. The 1D prediction of the dynamic response of the monopile with *L/D*=9 is later presented and discussed in Section 4.2.

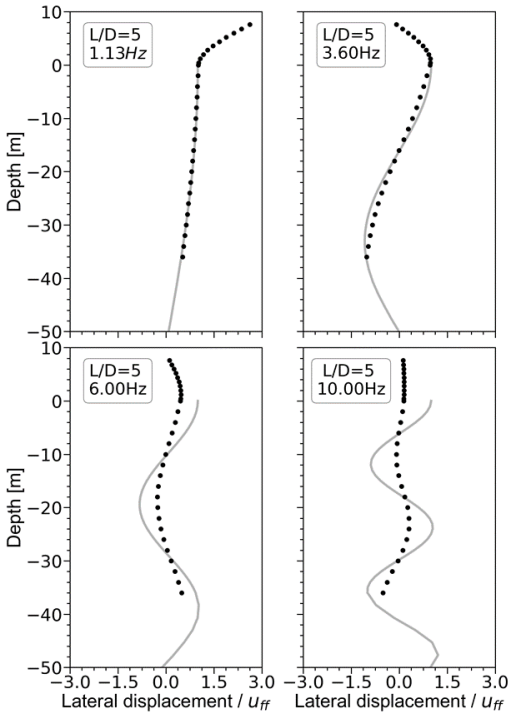

Figure 4: Free-field (grey solid line), monopile and structure on top (black dotted line) deformation over depth for *L/D*=5

4.2 *1D modelling with lateral p-y and rotational m-θ springs*

In this section, additional distributed *m-θ* springs are considered for modelling the dynamic soil-structure interaction in case of the monopiles with *L/D*=9 and 5.

Figure 5 presents both the pile head deflection and rotation interaction factors at steady-state versus the excitation frequency. In case of *L/D*=9, five different 1D calculations are presented, which account

for the two cases of calibrated k_y values (Section 3.1; Figure 2) and the three k_y-k_θ stiffness combinations previously presented in Section 3.2.

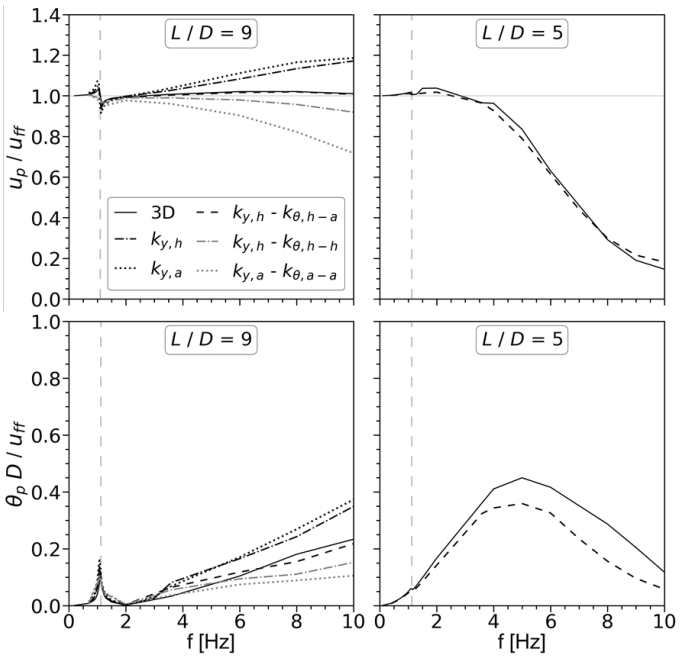

Figure 5: Dynamic response in terms of pile head response for L/D=9 (left) and L/D=5 (right) when p-y and m-θ springs are used

Similarly to Figure 3, local amplification and de-amplification of u_p relative to u_{ff} occur around $f_{0,SSI}$. As already discussed, this is owing to the inertial loading of the structure on top. Regarding the rotational dynamic interaction factor θ_p D / u_{ff}, a local amplification takes place at $f_{0,SSI}$, owing to the system being at resonance.

However, it is observed that given the same structure properties on top and the lower geometrical rigidity of the monopile with L/D=9, in comparison to the one with L/D=5, higher inertial effects take place (i.e., greater local amplification/de-amplification of u_p / u_{ff} and higher local amplification of θ_p D / u_{ff} around $f_{0,SSI}$).

On the other hand, for high excitation frequencies and short wavelengths, the higher L/D value results in the kinematic interaction between the soil and the monopile being lower for L/D=9 than L/D=5. In case of L/D=5, u_p / u_{ff} is lower than 1, which is justified by the significant kinematic interaction and the resulting deformation pattern shown in Figure 4. However, in case of L/D=9, u_p is practically constant and equal to u_{ff} for frequencies higher than $f_{0,SSI}$. Yet, the kinematic effects are more significant for L/D=9 than for L/D=26, which is also justified by the fact that the use of p-y springs only over-predicts the dynamic response, implying that additional resistant mechanisms are of importance, similarly to the monopile with L/D=5.

The k_y and k_θ spring stiffness values that optimize the match between the 3D and 1D FE calculations for both dynamic interaction factors in case of L/D=9 are the ones which account for the pile head deflection ($k_{y,h}$) and the average-over-depth monopile rotation ($k_{\theta,h\text{-}a}$), respectively. The same is true in case of L/D=5; this is why the results for the 1D FE model which makes use of the spring stiffnesses $k_{y,h}$ and $k_{\theta,h\text{-}a}$ are presented only.

As already seen, $k_{y,h}$ results in better agreement with 3D around $f_{0,SSI}$, for both L/D=26 and 5, given the significance of the inertial interaction effects (i.e., pile head loading that stresses the pile close the surface, Section 4.1) and the low kinematic effects for the systems examined in this report (Figure 4). On the other hand, the kinematic interaction effects, which are defined as the interaction between the soil layer and monopile over the pile embedded depth, become more important as the excitation frequency increases and the wavelength decreases (Figure 4). Hence, it is no surprise that calibrating k_θ based on the average-over-depth rotation (while accounting for $k_{y,h}$) betters the match between 3D and 1D especially for frequencies higher than $f_{0,SSI}$.

4.3 *1D modelling including the base shear and moment*

The base shear and moment effect are examined in terms of the monopile moment and shear force profiles for a mono-harmonic base excitation with frequency 1.20Hz (i.e., first natural frequency of the soil layer, where the maximum pile head displacement occurs). This is done for the rigid monopiles with L/D equal to 5 and 9, as presented in Figure 6.

First, a base translational and subsequently a base rotational spring are employed to examine their relative effect on the predictions of the 1D FE models. In case of the distributed lateral and rotational springs, the set of spring stiffness values which give the best 3D-to-1D fit, as defined in Section 4.2, are applied.

The base lateral and rotational spring stiffnesses, herein denoted by $K_{y,base}$ and $K_{\theta,base}$, are defined as proportional to (G_{soil} D) and (G_{soil} D^3), respectively, according to the formulas for surface circular foundations presented in Varun et al. (2009). No stiffness variation with L/D is considered. It should be noted that the aim of the present study is to examine the effect of the base soil reaction mechanisms on the system's response, not to provide a calibration strategy.

According to Figure 6, the 3D base shear and moment values are lower for L/D=9 than for L/D=5, as also reported by He et al. (2021). This is attributed to the influence of the bigger diameter for the monopile with L/D=5 in comparison to the monopile with L/D=9 (Table 1).

Regarding the contribution of the base translational and rotational springs to the predictions of the 1D FE models, it is observed that, for both monopiles, the base shear predictions improve when the base lateral spring is employed, while to capture the

base moment, a base rotational spring is needed. Given that the herewith assigned values do not capture the 3D values of base shear and moment, calibration procedures should be examined. Similar observations are made with regard to different excitations frequencies (Delavinia, 2022).

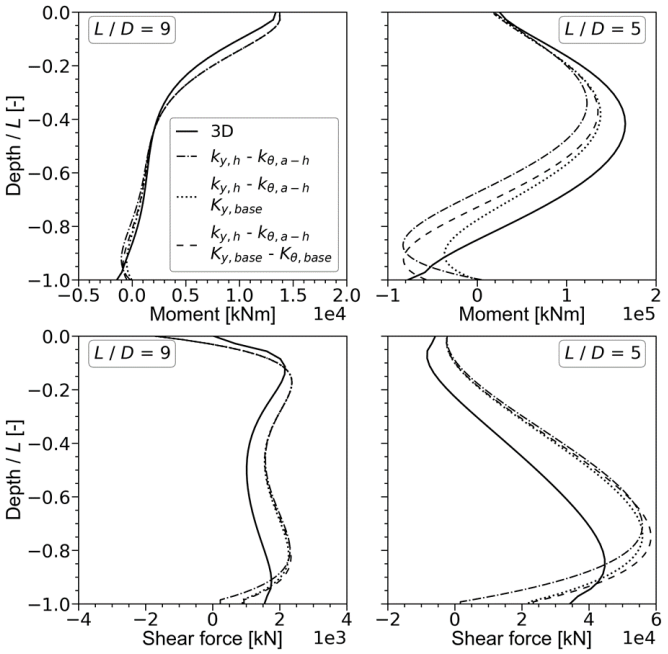

Figure 6: Moment and shear force profile in case of a mono-harmonic base excitation of 1.20Hz, for *L/D*=9 (left) and *L/D*=5 (right)

5 Case study

In this section, the previously defined distributed spring stiffness values ($k_{y,h}$ and $k_{\theta,h\text{-}a}$, Section 4.2) are employed to examine the 1D transient response of the soil-structure system in case of the monopile with *L/D*=5 under the Kobe 1995 TAK000 (Takatori) component, obtained from OpenSeesPL. Please, note that the base reaction components are omitted. Figure 7 shows the pile head deflection relative to the bottom of the soil layer (herewith denoted as U_p) and rotation (denoted by Θ_p) variation with time in case of the monopile with *L/D*=5.

As shown in this figure, the 1D prediction of the seismic response for *L/D*=5 matches adequately well the 3D. This is attributed to the good prediction of the examined steady-state dynamic response by the hereby employed 1D FE model and the satisfying prediction of the first natural frequency of the system (Figure 5).

A similarly good agreement between 3D and 1D response has also been observed in case of the monopile with *L/D*=9 – not reported here for brevity. Nevertheless, the underprediction of the first natural frequency of the system with *L/D*=26 (Section 3.1) results in a mismatch between 3D and 1D of the transient pile head response under seismic loading. The 1D transient response of the monopiles with *L/D*=26 and 9 are presented in Delavinia (2022).

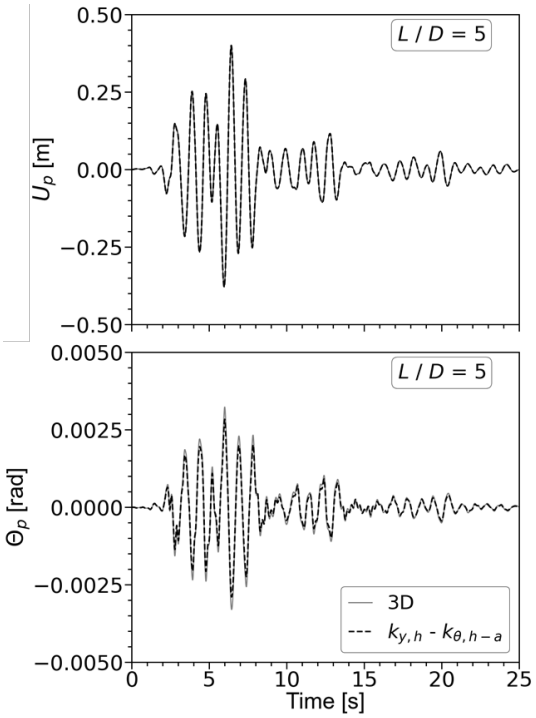

Figure 7: Pile head lateral deflection (top) and rotation (bottom) with time in case of the monopile with *L/D*=5 under the Kobe 1995 earthquake loading (TAK000 component, as obtained from OpenSeesPL)

6 Conclusions

This study concerns the 1D modelling of the soil-structure seismic interaction under the assumption of linear elasticity, for three different monopile *L/D* ratios. The 1D models have been based on the BWF approach, where the monopile is supported by distributed *p-y* springs. In addition to this, the contributions of the following three reaction components have been assessed: distributed moment-rotation, base lateral, and base moment reactions.

In the case of the uniformly distributed *p-y* and *m-θ* springs, different calibration procedures have been examined (Section 3). The linear spring stiffness values were employed throughout the examined frequency range under mono-harmonic base excitations, and the calibration methods that minimize the 3D-to-1D mismatch were defined (Section 4). Lastly, the 1D seismic response in case of a realistic earthquake excitation of the soil-structure system with a monopile of *L/D*=5 was compared with the 3D results (Section 5). The main conclusions are summarized below:

- The monotonically defined normalized *p-y* spring stiffness k_y / G_{soil} increases as *L/D* decreases (Figure 2), in agreement with previous literature;
- The monotonically determined normalized *m-θ* spring stiffness k_θ / (G_{soil} D^2) is independ-

ent of *L/D* for the two rigid monopiles examined herein, with *L/D*=9 and 5, in contrast to literature findings (Table 2);

- For the slender monopile with *L/D*=26, the monotonically calibrated distributed *p-y* springs under-predict the first natural frequency of the system (Figure 3);
- For the stubbier monopiles with *L/D*=9 and 5, the use of distributed *p-y* and *m-θ* springs, monotonically calibrated based on the pile head deflection and average-over-depth rotation ($k_{y,h}$ and $k_{\theta,h\text{-}a}$), results in a good agreement between the 3D and 1D calculations of the first natural frequency of the system and the pile head response no matter the excitation frequency (Figure 5, Figure 7);
- The base shear and moment effects are more prominent in case of *L/D*=5 (*D*=7.5m) than for *L/D*=9 (*D*=2.0m) (Figure 6). To capture adequately the moment and shear force profiles, the use of a base translational and rotational spring should be considered – with corresponding calibration recipes to be further refined in the future.

7 References

Anoyatis G, Di Laora R, Mandolini A and Mylonakis G. (2013). Kinematic response of single piles for different boundary conditions: Analytical solutions and normalization schemes. Soil Dynamics and Earthquake Engineering 44: 183–195.

API. (2011). Recommended Practice 2GEO Geotechnical and Foundation Design Considerations. American Petroleum Institute.

Bhattacharya S, Biswal S, Aleem M, Amani S, Prabhakaran A, Prakhya G, Lombardi D and Mistry HK. (2021). Seismic design of offshore wind turbines: Good, bad and unknowns. Energies 14.

Boulanger RW, Curras CJ, Kutter BL, Wilson DW and Abghari A. (1999). Seismic soil-pile-structure interaction experiments and analyses. Journal of Geotechnical and Geoenvironmental Engineering 125(9): 750–759.

Byrne BW, McAdam R, Burd HJ, Houlsby GT, Martin CM, Zdravković L, Taborda DMG, Potts DM, Jardine RJ, Sideri M, Schroeder FC, Gavin K, Doherty P, Igoe D, Muir Wood A, Kallehave D and Skov Gretlund, J. (2015). New design methods for large diameter piles under lateral loading for offshore wind applications. Proc. Int. Symp. Frontiers in Offshore Geotechnics, ISFOG 2015. Oslo, Norway.

Dafalias YF and Manzari MT. (2004). Simple plasticity sand model accounting for fabric change effects. Journal of Engineering Mechanics 130(6): 622–634.

Delavinia D. (2022). Seismic response of monopile foundations for offshore wind turbines: from 3D to 1D modelling of soil-foundation interaction. Master thesis. Delft University of Technology.

DNVGL. (2016). Support structures for wind turbines. Det Norske Veritas. DNVGL-ST-0126.

Fan K and Gazetas G. (1991). Seismic response of single piles and pile groups. National Center For Earthquake Engineering Research. Technical Report NCEER-91-0003.

Gazetas G. (1984). Seismic response of end-bearing single piles. Soil Dynamics and Earthquake Engineering 3(2).

Gazetas G and Dobry R. (1984). Horizontal response of piles in layered soils. Journal of Geotechnical Engineering 110(1): 20–40.

Gerolymos N and Gazetas G. (2006). Winkler model for lateral response of rigid caisson foundations in linear soil. Soil Dynamics and Earthquake Engineering 26: 347–361.

GWEC (2022, April). Global Wind Report 2022.

Griffiths DV. (1989). Advantages of consistent over lumped methods for analysis of beams on elastic foundations. Communications in applied numerical methods 5: 53–60.

He R, Kaynia AM and Zhu T. (2021). Effect of base shear and moment on lateral dynamic behavior of monopiles. Ocean Engineering 228.

Kaynia AM. (2020). Effect of kinematic interaction on seismic response of offshore wind turbines on monopiles. Earthquake Engineering and Structural Dynamics 50: 777–790.

Kementzetzidis E, Pisanò and Metrikine AV. (2022). A memory-enhanced p-y model for piles in sand accounting for cyclic ratcheting and gapping effects. Computers and Geotechnics 148.

Kementzetzidis E. (2023). Cyclic behaviour of laterally loaded (mono)piles in sand: With emphasis on pile driving effects. Doctoral dissertation. Delft University of Technology.

Lu J, Elgamal A and Yang Z. (2011). OpenSeesPL: 3D Lateral Pile-Ground Interaction, User Manual, Beta 1.0.

McKenna F, Scott MH and Fenves GL. (2010). Nonlinear finite-element analysis software architecture using object composition. Journal of Computing in Civil Engineering 24(1):95-107.

Medina C, ´Alamo GM and Quevedo-Reina R. (2021). Evolution of the seismic response of monopile-supported offshore wind turbines of increasing size from 5 to 15 mw including dynamic soil-structure interaction. Journal of Marine Science and Engineering 9.

Rahmani A, Taiebat M, Liam Finn WD and Ventura CE. (2018). Evaluation of p-y springs for nonlinear static and seismic soil-pile interaction analysis under lateral loading. Soil Dynamics and Earthquake Engineering 115: 438–447.

Randolph M and Gourvenec S. (2011). Offshore Geotechnical Engineering. Taylor & Francis.

Tsetas A, Tsouvalas A, Gómez SS, Pisanò F, Kementzetzidis E, Molenkamp T, Elkadi ASK and Metrikine AV. (2023). Gentle Driving of Piles (GDP) at a sandy site combining axial and torsional vibrations: Part I - installation tests. Ocean Engineering 270.

Turner BJ, Brandenberg SJ and Stewart JP. (2017). Influence of kinematic SSI on foundation input motions for bridges on deep foundations. Pacific Earthquake Engineering Research Center. PEER Report No. 2017/08.

Vacareanu V, Kementzetzidis E and Pisanò F. (2019). 3D FE seismic analysis of a monopile-supported offshore wind turbine in a non-liquefiable soil deposit. Proc. 2nd Int. Conf. on Natural Hazards & Infrastructure, ICONHIC 2019. Chania, Greece, 23–26.

Varun, Assimaki D and Gazetas G. (2009). A simplified model for lateral response of large diameter caisson foundations—linear elastic formulation. Soil Dynamics and Earthquake Engineering 29: 268–291.

Wan X, Doherty JP and Randolph MF. (2021). Relationships between lateral and rotational load transfer stiffnesses and soil modulus for the elastic response of monopiles. Computers and Geotechnics 137.

Watanabe K, Pisanò F and Jeremić B. (2017). Discretization effects in the finite element simulation of seismic waves in elastic and elastic-plastic media. Engineering with Computers 33: 519–545.

Wind Europe (2020, February). Offshore Wind in Europe: Key trends and statistics 2019.